

Space Object Classification and Characterization Via Multiple Model Adaptive Estimation

Richard Linares

Director's Postdoctoral Fellow

Space Science and Applications, ISR-1
Los Alamos National Laboratory, MS D466
Los Alamos, NM 87545
linares@lanl.gov

John L. Crassidis

CUBRC Professor

in Space Situational Awareness
Dept. of Mech. & Aero. Eng.
University at Buffalo
State University of New York
Amherst, NY 14260-4400 U.S.A.
johnc@buffalo.edu

Moriba K. Jah

Mission Lead, Space Situational Awareness
U.S. Air Force Research Laboratory
Kirtland Air Force Base
Albuquerque, NM 87117

Abstract—In recent years there has been an increase in the number of inactive and debris objects in space. The characterization of the uncertainty in the knowledge of these Space Objects (SOs) is very important in developing an understanding of the space debris fields and any present or future threat they may pose. This work examines classification based on Multiple Model Adaptive Estimation (MMAE) to extract SO characteristics from observations while estimating the probability the observations belong to a given class of objects. Recovering these characteristics and trajectories with sufficient accuracy is shown in this paper, where the characteristics are inherent in unique SO models used in the MMAE filter bank. A number of scenarios are shown to highlight the effectiveness of the proposed classification approach. The performance of this strategy is demonstrated via simulated scenarios.

I. INTRODUCTION

Due to the large number of space objects (SOs) and the limited number of sensors available to track them, it is difficult to maintain persistent surveillance, and, therefore, there is inherent uncertainty and latency in the knowledge of the SO population. Although the amount of light collected from these objects is small, information can still be extracted from photometric data which can be used to determine shapes and other properties. Light curve data are the time-varying sensor wavelength-dependent apparent magnitude of energy (e.g. photons) scattered (reflected) off of an object along the line-of-sight to an observer. Attitude estimation and extract of other characteristic using light curve data has been demonstrated in Refs. 1–6.

An approach is presented that uses the probability from a Multiple Model Adaptive Estimation (MMAE) process to determine the probability that a given Space Object (SO) falls in a given class. MMAE is a recursive algorithm that uses a bank of estimators, each dependent on a particular hypothesis, to determine an estimate based upon an unknown physical process under consideration. In particular, the hypotheses can correspond to different mathematical models of the same physical process or of the same model but dependent upon different constants or model parameters. The classification approach used in the work is outlined in Figure 1. The first determination is made from the size of the shape models in the bank. For each model in the bank an aspect ratio is calculated

for each size by calculating the length ratio of that side with respect to the largest side and if a given model has an aspect ratio less than 0.1 it is considered to be a fragment.

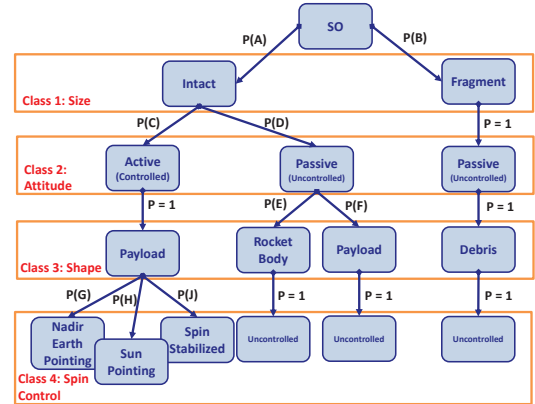


Fig. 1: Overview of Classification Approach

The second classification determination is made from the control states. For each model in the bank that is not a fragment or a rocket body additional models are created that are copies of that shape model but have different control profiles. The control profiles include uncontrolled, Sun pointing, spin stabilized, and nadir pointing. Therefore, for models that are not fragments of rocket bodies 3 additional modes are created with control. The control states are not limited to ones used in this work and large list of control state may be possible but for this study these three are sufficient.

The classification is determined using the shape model, for example determining whether an object is intact or passive and whether it is a rocket body or a payload. The final classification further separates the SO into the type of control state and determining whether an object is uncontrolled or Sun pointing, etc. This method uses the MMAE probability to classify the four feature classes and results for this method are shown. This paper discusses the theory involved behind the algorithm and results from a variety of simulation trials are shown.

The organization of this paper is as follows. First, the

Ashikhmin-Shirley light curve model is shown, and the kinematic and dynamic models used in this work are discussed. Next, the Unscented Kalman Filter approach used in this work is outlined. Following this, the MMAE approach used in this work is outlined. Then the classification approach is discussed. Finally, results are shown for simulated examples. Discussions and conclusions are provided.

II. ASHIKHMIN-SHIRLEY MODEL

Figure 2 shows the space object shape model and reflection geometry. In addition to the azimuth and elevation, the optical site also records the magnitude of the brightness of the Space Objects (SOs). The brightness of an object in space can be modeled using an anisotropic Phong light diffusion model or the Ashikhmin-Shirley model.⁷ This model is based on the bidirectional reflectance distribution function (BRDF) which models light distribution scattered from the surface due to the incident light. The BRDF at any point on the surface is a function of two directions, the direction from which the light source originates and the direction from which the scattered light leaves the observed surface. The model in Ref. 7 decomposes the BRDF into a specular component and a diffuse component. The two terms sum to give the total BRDF:

$$\rho_{\text{total}}(i) = \rho_{\text{spec}}(i) + \rho_{\text{diff}}(i) \quad (1)$$

where i denotes the i^{th} facet of the SOs. Each facet contributes independently to the brightness and total brightness is the sum over each facet's contribution. The diffuse component represents light that is scattered equally in all directions (Lambertian) and the specular component represents light that is concentrated about some direction (mirror-like). Reference 7 develops a model for continuous arbitrary surfaces but simplifies for flat surfaces. This simplified model is employed in this work as shape models are considered to consist of a finite number of flat facets. Therefore the total observed brightness of an object becomes the sum of the contribution from each facet. Under the flat facet assumption the specular term of the BRDF becomes⁷

$$\rho_{\text{spec}}(i) = \frac{\sqrt{(n_u(i) + 1)(n_v(i) + 1)}}{8\pi} \frac{(\mathbf{u}_n^I(i) \cdot \mathbf{u}_h^I)^z F_{\text{reflect}}(i)}{\mathbf{u}_n^I(i) \cdot \mathbf{u}_{\text{sun}}^I + \mathbf{u}_n^I(i) \cdot \mathbf{u}_{\text{obs}}^I - (\mathbf{u}_n^I(i) \cdot \mathbf{u}_{\text{sun}}^I)(\mathbf{u}_n^I(i) \cdot \mathbf{u}_{\text{obs}}^I)} \quad (2)$$

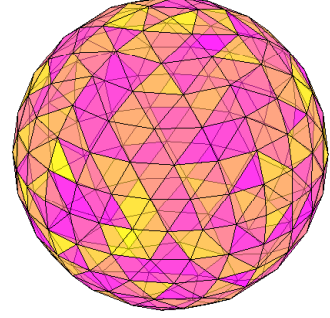
where the exponent z is given by

$$z = \frac{n_u(i)(\mathbf{u}_h^I \cdot \mathbf{u}_u^I(i))^2 + n_v(i)(\mathbf{u}_h^I \cdot \mathbf{u}_v^I(i))^2}{(1 - (\mathbf{u}_h^I \cdot \mathbf{u}_n^I(i))^2)} \quad (3)$$

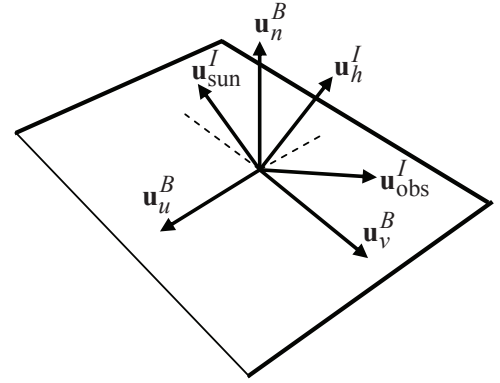
where the Fresnel reflectance is given by

$$F_{\text{reflect}}(i) = R_{\text{spec}}(i) + (1 - R_{\text{spec}}(i))(1 - \mathbf{u}_{\text{sun}}^I \cdot \mathbf{u}_h^I)^5 \quad (4)$$

where R_{spec} is the specular reflectance coefficient. The parameters of the Phong model that dictate the directional (locally horizontal or vertical) distribution of the specular terms are n_u and n_v . The terms in Eq. (2) are functions of the reflection geometry which is described in Figure 2(b). The diffuse term



(a) Space Object Shape Model



(b) Reflection Geometry

Fig. 2: Reflection Geometry and Space Object Shape Model

of the BRDF is

$$\rho_{\text{diff}}(i) = \left(\frac{28R_{\text{diff}}(i)}{23\pi} \right) (1 - R_{\text{spec}}(i)) \cdot \left[1 - \left(1 - \frac{\mathbf{u}_n^I(i) \cdot \mathbf{u}_{\text{sun}}^I}{2} \right)^5 \right] \left[1 - \left(1 - \frac{\mathbf{u}_n^I(i) \cdot \mathbf{u}_{\text{obs}}^I}{2} \right)^5 \right] \quad (5)$$

where $R_{\text{diff}}(i)$ is the diffuse coefficient for the i^{th} side. The model discussed above assumes only single scattering and no self shadowing.

A. Flux Calculation

The apparent magnitude of an SO is the result of sunlight reflecting off of its surfaces along the line-of-sight to an observer. First, the fraction of visible sunlight that strikes an object (and is not absorbed) is computed by

$$F_{\text{sun}}(i) = C_{\text{sun,vis}} (\mathbf{u}_n^I(i) \cdot \mathbf{u}_{\text{sun}}^I) \quad (6)$$

where $C_{\text{sun,vis}} = 1062 \text{ W/m}^2$ is the power per square meter impinging on a given object due to visible light striking the surface. If either the angle between the surface normal and the observer's direction or the angle between the surface normal and Sun direction is greater than $\pi/2$ then there is no light reflected toward the observer. If this is the case then the fraction of visible light is set to $F_{\text{sun}}(i) = 0$. Next, the fraction of sunlight that strikes an object that is reflected must be computed:

$$F_{\text{obs}}(i) = \frac{F_{\text{sun}}(i) \rho_{\text{total}}(i) \mathcal{A}(i) (\mathbf{u}_n^I(i) \cdot \mathbf{u}_{\text{obs}}^I)}{\|\mathbf{d}^I\|^2} \quad (7)$$

The reflected light of each facet is now used to compute the total photon flux, which is measured by an observer:

$$\tilde{F} = \left[\sum_{i=1}^N F_{\text{obs}}(i) \right] + v_{\text{CDD}} \quad (8)$$

where v_{CDD} is the measurement noise associated with flux measured by a Charge Coupled Device (CCD) sensor. The total photon flux is then used to compute the apparent brightness magnitude

$$m_{\text{app}} = -26.7 - 2.5 \log_{10} \left| \frac{\tilde{F}}{C_{\text{sun,vis}}} \right| \quad (9)$$

where -26.7 is the apparent magnitude of the Sun.

B. Unscented Kalman Filter

The attitude state errors are represented as error Generalized Rodrigues Parameters (GRPs) resulting in a minimum parameter representation for the attitude state error.⁸ To within first order, the state error covariance of the attitude is invariant whether the errors are parameterized using quaternions or GRPs.⁹ Therefore, the attitude state error-covariance can be directly decomposed into error GRP sigma points for use in the Unscented Kalman Filter (UKF). The sigma points corresponding to the error GRPs are first converted into error quaternions so that the quaternion sigma points can be computed. The error quaternion, denoted by $\delta \mathbf{q}_k^-(i)$, associated with the i^{th} error GRP sigma point is computed by⁸

$$\delta \boldsymbol{\varrho}_k^-(i) = f^{-1} [a + \delta q_{4_k}^-(i)] \boldsymbol{\chi}_k^{\delta p}(i) \quad (10a)$$

$$\delta q_{4_k}^-(i) = \frac{-a \|\boldsymbol{\chi}_k^{\delta p}(i)\|^2 + f \sqrt{f^2 + (1 - a^2) \|\boldsymbol{\chi}_k^{\delta p}(i)\|^2}}{f^2 + \|\boldsymbol{\chi}_k^{\delta p}(i)\|^2} \quad (10b)$$

$$\delta \mathbf{q}_k^-(i) = \begin{bmatrix} \delta \boldsymbol{\varrho}_k^-(i) \\ \delta q_{4_k}^-(i) \end{bmatrix} \quad (10c)$$

where a is a parameter from 0 to 1 and f is a scale factor, which is often set to $f = 2(a + 1)$ so that the attitude error covariance is that of the small roll, pitch and yaw angle errors. Here it is noted that the subscript I and superscript B in \mathbf{q}_I^B and its estimates are omitted in this and the following sections for clarity. The i^{th} quaternion sigma point is given by a rotation of $\delta \mathbf{q}_k^-(i)$ about the *a priori* estimate:

$$\hat{\mathbf{q}}_k^-(i) = \delta \mathbf{q}_k^-(i) \otimes \hat{\mathbf{q}}_k^-(0) \quad (11)$$

where

$$\mathbf{q}_1 \otimes \mathbf{q}_2 \equiv [\Psi(\mathbf{q}_1) \quad \mathbf{q}_1] \mathbf{q}_2 \quad (12)$$

The sigma points are propagated through the system dynamics:

$$\dot{\boldsymbol{\chi}}(i) = \mathbf{f}(\boldsymbol{\chi}(i), \hat{\mathbf{q}}(i)) \quad (13)$$

where

$$\mathbf{f}(\boldsymbol{\chi}, \hat{\mathbf{q}}) = \begin{bmatrix} \frac{1}{2} \Xi(\hat{\mathbf{q}}) \hat{\boldsymbol{\omega}} \\ J_{\text{SO}}^{-1} \left(\hat{\mathbf{T}}_{\text{srp}}^B - [\hat{\boldsymbol{\omega}} \times] J_{\text{SO}} \hat{\boldsymbol{\omega}} \right) \\ \hat{\mathbf{v}}^I \\ -\frac{\mu}{\hat{r}^3} \hat{\mathbf{r}}^I + \hat{\mathbf{a}}_{J_2} + \hat{\mathbf{a}}_{\text{SRP}}^I \end{bmatrix} \quad (14)$$

The estimated acceleration and torque due to SRP are calculated with equations given in Ref. 3, respectively. After propagation, the sigma points for the error GRP states are computed with the propagated attitude sigma points. The estimated mean sigma point quaternion, $\hat{\mathbf{q}}_{k+1}^-(0)$, is stored, and error quaternions corresponding to each propagated quaternion sigma point are computed as:

$$\delta \hat{\mathbf{q}}_{k+1}^-(i) = \hat{\mathbf{q}}_{k+1}^-(i) \otimes [\hat{\mathbf{q}}_{k+1}^-(0)]^{-1} \quad (15)$$

where the notation for the conjugate quaternion is defined as:

$$\mathbf{q}^{-1} \equiv \begin{bmatrix} -\boldsymbol{\varrho} \\ q_4 \end{bmatrix} \quad (16)$$

Using the result of Eq. (15), the error GRP sigma points are computed as

$$\delta \mathbf{p}_{k+1}^-(i) = f \frac{\delta \hat{\boldsymbol{\varrho}}_{k+1}^-(i)}{a + \delta \hat{q}_{4_{k+1}}^-(i)} \quad (17)$$

After setting the error GRP for the mean sigma point to zero, the propagated sigma points are reconstructed. The propagated mean and covariance are calculated as a weighted sum of the sigma points as

$$P_{k+1}^- = \sum_{i=0}^{2L} W_i^{\text{cov}} [\boldsymbol{\chi}_{k+1}(i) - \hat{\mathbf{x}}_{k+1}^-] [\boldsymbol{\chi}_{k+1}(i) - \hat{\mathbf{x}}_{k+1}^-]^T + Q_{k+1} \quad (18)$$

$$\hat{\mathbf{x}}_{k+1}^- = \sum_{i=0}^{2L} W_i^{\text{mean}} \boldsymbol{\chi}_{k+1}(i) \quad (19)$$

where Q_{k+1} is the discrete-time process noise covariance.

As previously discussed, measurements are available in the form of azimuth, elevation and apparent brightness magnitude, $\tilde{\mathbf{y}} \equiv [\tilde{m}_{\text{app}} \quad \tilde{a}_z \quad \tilde{e}_l]^T$. Estimated observations are computed for each sigma point using the observation models:

$$\mathbf{y}_k(i) = \mathbf{h}[\boldsymbol{\chi}_k(i), \hat{\mathbf{q}}_k^-(i)] \quad (20)$$

The mean estimated output and covariance matrices are then calculated. The quaternion update is performed by converting the error GRP states of $\hat{\mathbf{x}}_k^+$ to a quaternion, $\delta \hat{\mathbf{q}}_k^+$, via Eq. (10), and performing

$$\hat{\mathbf{q}}_k^+ = \delta \hat{\mathbf{q}}_k^+ \otimes \hat{\mathbf{q}}_k^-(0) \quad (21)$$

C. Multiple Model Adaptive Estimation

In this section a review of MMAE is shown. More details can be found in Refs. 10 and 11. Figure 3 shows the MMAE

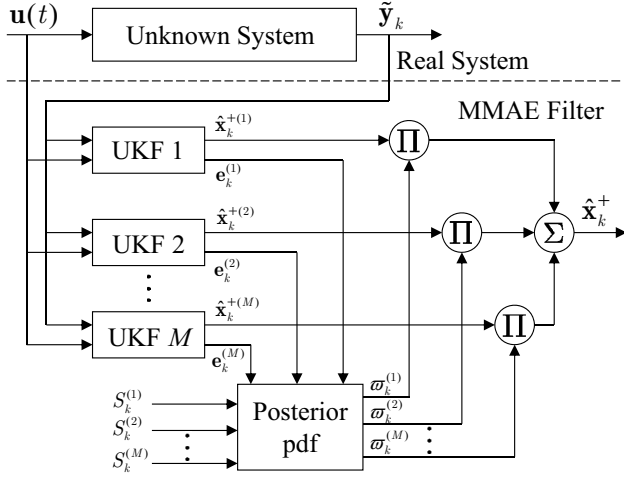


Fig. 3: MMAE Process

process. Multiple-model adaptive estimation is a recursive estimator that uses a bank of filters that depend on models with different parameters, denoted by the vector \mathbf{p} , which is assumed to be constant (at least throughout the interval of adaptation). Note the stationary assumption for the state and/or output processes is not necessarily required though, i.e. time varying state and output matrices can be used. A set of distributed elements is generated from some known pdf of \mathbf{p} , denoted by $\Pr(\mathbf{p})$, to give $\{\mathbf{p}^{(\ell)}; \ell = 1, \dots, M\}$. The finite set of parameters can be the results of discretizing a continuous parameters space, selecting a set of values $\{\mathbf{p}^{(1)}, \mathbf{p}^{(2)}, \dots, \mathbf{p}^{(k)}\}$ dispersed throughout the region of reasonable parameter values.

The goal of the estimation process is to determine the conditional probability of the ℓ^{th} element, $\mathbf{p}^{(\ell)}$, given all the measurements. Application of Bayes' rule yields

$$\Pr(\mathbf{p}^{(\ell)}|\tilde{\mathbf{Y}}_k) = \frac{\Pr(\tilde{\mathbf{Y}}_k|\mathbf{p}^{(\ell)}) \Pr(\mathbf{p}^{(\ell)})}{\sum_{j=1}^M \Pr(\tilde{\mathbf{Y}}_k|\mathbf{p}^{(j)}) \Pr(\mathbf{p}^{(j)})} \quad (22)$$

where $\tilde{\mathbf{Y}}_k$ denotes the sequence $\{\tilde{\mathbf{y}}_0, \tilde{\mathbf{y}}_1, \dots, \tilde{\mathbf{y}}_k\}$. The conditional probability $\Pr(\mathbf{p}^{(\ell)}|\tilde{\mathbf{Y}}_k)$ will be the metric used to select the most likely model and/or the most likely combination of shape models. The *a posteriori* probabilities can be computed through¹²

$$\begin{aligned} \Pr(\mathbf{p}^{(\ell)}|\tilde{\mathbf{Y}}_k) &= \frac{\Pr(\tilde{\mathbf{y}}_k, \mathbf{p}^{(\ell)}|\tilde{\mathbf{Y}}_{k-1})}{\Pr(\tilde{\mathbf{y}}_k|\tilde{\mathbf{Y}}_{k-1})} \\ &= \frac{\Pr(\tilde{\mathbf{y}}_k|\hat{\mathbf{x}}_k^{-(\ell)}) \Pr(\mathbf{p}^{(\ell)}|\tilde{\mathbf{Y}}_{k-1})}{\sum_{j=1}^M \left[\Pr(\tilde{\mathbf{y}}_k|\hat{\mathbf{x}}_k^{-(j)}) \Pr(\mathbf{p}^{(j)}|\tilde{\mathbf{Y}}_{k-1}) \right]} \quad (23) \end{aligned}$$

The conditional probability of the observations based on each hypothesis (likelihood),

$p(\tilde{\mathbf{y}}_k|\hat{\mathbf{x}}_k^{-(\ell)})$ are given as

$$\Pr(\tilde{\mathbf{y}}_k|\hat{\mathbf{x}}_k^{-(\ell)}) = \frac{1}{\det(2\pi S_k^{(\ell)})^{1/2}} \exp \left\{ -\frac{1}{2} \mathbf{e}_k^{(\ell)T} S_k^{(\ell)-1} \mathbf{e}_k^{(\ell)} \right\} \quad (24)$$

where measurement residual for the ℓ^{th} hypothesis (model) is given by

$$\mathbf{e}_k^{(\ell)} = \tilde{\mathbf{y}}_k - \mathbf{h}[\hat{\mathbf{x}}_k^{-(\ell)}] \quad (25)$$

and corresponding residual covariance matrix from the UKFs

$$S_k^{(\ell)} = P_k^{vv(\ell)} \quad (26)$$

where $P_k^{vv(\ell)}$ is the innovation matrix for the ℓ^{th} filter.

Note that the denominator of Eq. (23) is just a normalizing factor. The recursion formula can now be cast into a set of defined weights $\varpi_k^{(\ell)}$, so that

$$\begin{aligned} \varpi_k^{(\ell)} &= \varpi_{k-1}^{(\ell)} \Pr(\tilde{\mathbf{y}}_k|\hat{\mathbf{x}}_{k-1}^{-(\ell)}) \\ \varpi_k^{(\ell)} &\leftarrow \frac{\varpi_k^{(\ell)}}{\sum_{j=1}^M \varpi_k^{(j)}} \quad (27) \end{aligned}$$

where $\varpi_k^{(\ell)} \equiv \Pr(\mathbf{p}^{(\ell)}|\tilde{\mathbf{Y}}_k)$. Note that only the current time measurement $\tilde{\mathbf{y}}_k$ is needed to update the weights. The weights at time t_0 are initialized to $\varpi_0^{(\ell)} = 1/M$ for $\ell = 1, 2, \dots, M$. The convergence properties of MMAE are shown in Ref. 12, which assumes ergodicity in the proof. The ergodicity assumptions can be relaxed to asymptotic stationarity and other assumptions are even possible for non-stationary situations.¹³

From Eq. (24) and Eq. (27) it is seen that models which have lower residuals will have probability that will increase; this will favor models that fit the observations better. Also from Eq. (24) it is seen that models which have small values for $\det(S_k^{(\ell)})$ will have probability that will grow. Assuming that all models have same measurement noise covariance matrix R_k , this will favor models that have smaller variance. Therefore the MMAE process will tend to select the maximum likelihood (minimum variance) model from the bank of models.

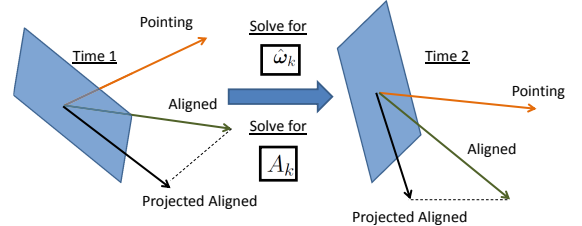


Fig. 4: Overview of Angular Velocity Determination Approach

D. Angular Velocity Determination

When processing light curve observations it may not be valid to assume that the SO is uncontrolled and therefore we must take into account the possibility of controlled attitude states. Determining whether a SO has active control or not may

also provide a feature state that may be used for classification. For example, a determination of whether a SO is passive or active can be made based on whether light curve observations indicated that the SO has active attitude control.

In this work, the attitude control is simulated by assuming control profiles, for example Sun pointing, Nadir pointing, and spin stabilized. Then for each control profile a desired angular velocity is determined which will allow the SO to track the relevant directions. The angular velocity profiles are used to calculate the torque required to track this profile. This section discusses the attitude control approach used and four method for calculating the desired angular velocity profile which is shown in Figure 4. The attitude control is designed to minimize the following error:

$$\mathbf{e} = \boldsymbol{\omega} - \boldsymbol{\omega}_d \quad (28)$$

Differentiating this equation with respect to time yields

$$\dot{\mathbf{e}} = \dot{\boldsymbol{\omega}} - \dot{\boldsymbol{\omega}}_d \quad (29)$$

It is desirable for the error dynamics to decay exponential over time, i.e. $\mathbf{e} \propto e^{-k_p t}$, and therefore the error rate equation is desired to have the following form:

$$\dot{\mathbf{e}} = -k_p \mathbf{e} \quad (30)$$

Then using Euler's equation and assuming disturbance torques are negotiable, Eq. (29) can be written as

$$\dot{\mathbf{e}} = J_{SO}^{-1} (\boldsymbol{\tau} - [\boldsymbol{\omega} \times] J_{SO} \boldsymbol{\omega}) - \dot{\boldsymbol{\omega}}_d \quad (31)$$

where $\boldsymbol{\tau}$ is the torque provide by the attitude actuator. Then for an exponentially decaying tracking error the desired torque expression becomes

$$\boldsymbol{\tau} = -J_{SO}^{-1} (\boldsymbol{\tau} - [\boldsymbol{\omega} \times] J_{SO} \boldsymbol{\omega}) + \dot{\boldsymbol{\omega}}_d - k_p \mathbf{e} \quad (32)$$

This expression is used to calculate the torque required to maintain the desired pointing profile.

In this section angular velocity determination approaches are discussed. Consider the following unit-vector measurement model at time t_k :

$$\tilde{\mathbf{b}}_{j_k} = A_k \mathbf{r}_j + \mathbf{v}_{j_k} \quad (33)$$

where $\tilde{\mathbf{b}}_{j_k}$ is the j^{th} pointing vector in the inertia frame and is \mathbf{r}_j the same pointing vector in the body frame. The attitude matrix mapping from inertia to the body frame is denoted by A_k . Our goal is to determine the rate of change of this attitude matrix or the angular velocity. Taking the difference between successive measurements of Eq. (33) gives

$$\tilde{\mathbf{b}}_{j_{k+1}} - \tilde{\mathbf{b}}_{j_k} = [A_{k+1} - A_k] \mathbf{r}_j + \mathbf{v}_{j_{k+1}} - \mathbf{v}_{j_k} \quad (34)$$

We assume that the body angular velocity $\boldsymbol{\omega}$ is constant between t_k and t_{k+1} , and ignore terms higher than first order in $\boldsymbol{\omega} \Delta t$. With these assumptions the following first-order approximation can be used:¹⁴

$$A_{k+1} \approx \left[I_{3 \times 3} - \Delta t [\boldsymbol{\omega}_k \times] \right] A_k \quad (35)$$

In this case $\boldsymbol{\omega}_k$ is the *average* velocity, but this becomes less of a problem as the sampling interval decreases. Substituting Eq. (35) into Eq. (34) gives

$$\tilde{\mathbf{b}}_{j_{k+1}} - \tilde{\mathbf{b}}_{j_k} = -\Delta t [\boldsymbol{\omega}_k \times] A_k \mathbf{r}_j + \mathbf{v}_{j_{k+1}} - \mathbf{v}_{j_k} \quad (36)$$

Our goal is to determine an angular velocity estimate independent of attitude and the reference vectors. This is accomplished by solving Eq. (33) in terms of $A_k \mathbf{r}_i$ and substituting the resultant into Eq. (36), which yields

$$\frac{1}{\Delta t} [\tilde{\mathbf{b}}_{j_{k+1}} - \tilde{\mathbf{b}}_{j_k}] = [\tilde{\mathbf{b}}_{j_k} \times] \boldsymbol{\omega}_k + \mathbf{w}_{j_k} \quad (37)$$

where \mathbf{w}_{j_k} is the new effective measurement noise vector given by

$$\mathbf{w}_{j_k} \equiv [\boldsymbol{\omega}_k \times] \mathbf{v}_{j_k} + \frac{1}{\Delta t} [\mathbf{v}_{j_{k+1}} - \mathbf{v}_{j_k}] \quad (38)$$

Note that Δt will have finite values, since discrete-time measurements are assumed. Equation (37) can now be cast into a linear least-squares form for all measurement vectors, which leads to

$$\hat{\boldsymbol{\omega}}_k = \frac{1}{\Delta t} \left[\sum_{j=1}^{n_k} [\tilde{\mathbf{b}}_{j_k} \times]^T R_{j_k}^{-1} [\tilde{\mathbf{b}}_{j_k} \times] \right]^{-1} \sum_{j=1}^{n_k} [\tilde{\mathbf{b}}_{j_k} \times]^T R_{j_k}^{-1} (\tilde{\mathbf{b}}_{j_{k+1}} - \tilde{\mathbf{b}}_{j_k}) \quad (39)$$

where $\hat{\boldsymbol{\omega}}_k$ is the estimate of $\boldsymbol{\omega}_k$. For small Δt the propagated true value of \mathbf{b}_j can be given using Eq. (35):

$$\mathbf{b}_{j_{k+1}} \approx \{I_{3 \times 3} - \Delta t [\boldsymbol{\omega}_k \times]\} \mathbf{b}_{j_k} \quad (40)$$

Substituting Eq. (40) into Eq. (35), left multiplying by $[\mathbf{b}_{j_k} \times]^T$ and right multiplying by $[\mathbf{b}_{j_k} \times]$ gives

$$[\mathbf{b}_{j_k} \times]^T R_{j_k}^{-1} [\mathbf{b}_{j_k} \times] = \bar{\sigma}_j^{-2} [\mathbf{b}_{j_k} \times]^T [\mathbf{b}_{j_k} \times] \quad (41)$$

where $\bar{\sigma}_j^2 \equiv 2\sigma_j^2 / \Delta t^2$. Also, since $\mathbf{b}_{j_{k+1}}^T \mathbf{b}_{j_k} \approx 1$, it is easy to show that $[\mathbf{b}_{j_k} \times]^T R_{j_k}^{-1} (\mathbf{b}_{j_{k+1}} - \mathbf{b}_{j_k}) \approx \bar{\sigma}_j^{-2} [\mathbf{b}_{j_k} \times]^T \mathbf{b}_{j_{k+1}}$. Therefore, Eq. (39) is well approximated by

$$\hat{\boldsymbol{\omega}}_k = \frac{1}{\Delta t} \left[\sum_{j=1}^{n_k} \bar{\sigma}_j^{-2} [\tilde{\mathbf{b}}_{j_k} \times]^T [\tilde{\mathbf{b}}_{j_k} \times] \right]^{-1} \sum_{j=1}^{n_k} \bar{\sigma}_j^{-2} [\tilde{\mathbf{b}}_{j_k} \times]^T \tilde{\mathbf{b}}_{j_{k+1}} \quad (42)$$

where the measurements have again been substituted in place of their true values.

III. SIMULATION RESULTS

Four simulation scenarios are presented to show the performance of the MMAE based classification approach to classify an SO from magnitude and angles observations. In each scenario a different object is selected that falls into a different class. The objects selected are spin stabilized bus, uncontrolled bus, nadir pointing bus, and uncontrolled rocket body. All scenarios, an SO is in near geosynchronous orbit with orbital elements given by $a = 42,364.17$ km, $e = 2.429 \times 10^{-4}$, $i = 30$ deg, $\omega = \Omega = 0.0$ deg and $M_0 = 91.065$ deg. The simulation epoch is 15-March-2010 at 04:00:00 GST. The initial quaternion and angular rate of the SO are given by $\mathbf{q}_I^B \equiv [0.7041 \ 0.0199 \ 0.0896 \ 0.7041]^T$ and $\boldsymbol{\omega}_{B/I}^B = [206.26 \ 103.13 \ 540.41]^T$ deg/hr.

Brightness magnitude and angle observations are simulated using a ground station located at 20.71° North, 156.26° West longitude and 3,058.6 m altitude. Measurements constructed using instantaneous geometry are corrupted by zero-

mean Gaussian white noise with standard deviations of 1 arc-seconds on the azimuth observation, 1 arc-seconds on the elevation observation and 0.1 for the brightness magnitude.¹⁵ Observations are available every 5 seconds for one hour. The initial states for each filter are given by $\hat{\mathbf{q}}_I^B(t_0) = [0.7500 \ 0.0712 \ 0.0947 \ 0.6508]^T$ (a 10 degree attitude error), $\hat{\omega}_{B/I}^B(t_0) = [220.26 \ 117.13 \ 554.41]^T$, $\hat{\mathbf{a}}(t_0) = 42,364.148255 \text{ km}$, $\hat{\mathbf{e}}(t_0) = 2.4290 \times 10^{-4}$, $\hat{\mathbf{i}}(t_0) = 30.0083 \text{ deg}$, $\hat{\omega}(t_0) = -1.172 \text{ deg}$, $\hat{\Omega}(t_0) = 0.0 \text{ deg}$ and $\hat{M}_0(t_0) = 92.137 \text{ deg}$. Initial 3σ values are taken to be 20 deg for the attitude states, 72 (deg/hr) on the angular rates, 300 km on position and 3 (km/s) on velocity. The process noise for the UKFs are taken as $Q_k^{(\ell)} = 0$ for this proof of concept simulation.

A. Classification Results

Figure 5 shows the classification results for a spin stabilized bus. In this case the bus models are considered to be regular cuboids with aspect ratio larger than 0.1. As discussed in classification section there are a number of classes the classification approach determines, whether the SO belongs to these classes. The first class is whether the SO is intact or a fragment. In this case the true model is an intact bus and from Figure 5 we can see that this determination is made relatively quickly. The second determination is whether SO is active or passive, which is also shown in Figure 5. The active or passive decision is made using the probability of all active and passive models in the bank. We can see from Figure 5 that the active model gain achieves large probabilities after 0.2 hours.

Additional examples are shown for an uncontrolled bus (Figure 6), nadir pointing bus (Figure 7), and uncontrolled rocket body (Figure 8). The approach shows good performance for these examples for determining the correct class. From the figures it can be seen that some objects take longer to classify. This is due to the fact that for some spin states the light curves are similar, but for uncontrolled spin states the light curve differs significantly. This can be seen from nadir pointing bus (Figure 7), which takes the longest to converge to its classification, and from uncontrolled rocket body (Figure 8), which converges the fastest to its classification.

IV. CONCLUSION

In this paper, an Multiple Model Adaptive Estimation (MMAE) scheme for space object classification using light curve and angles data was presented, which can be used to identify the most probable class of the SO along with its associated rotational and translational states. Using an Unscented filter to reduce brightness magnitude and angle data, the MMAE is able to determine the probability of each model. An approach is presented that uses the probability from a MMAE process to determine the probability that a given Space Object (SO) falls in a given class. The classification approach determines whether the SO is intact or fragment, its control states, the type of control state, and whether it is rocket body, payload, or debris. Simulation results showed a number of examples and good results for classification are given.

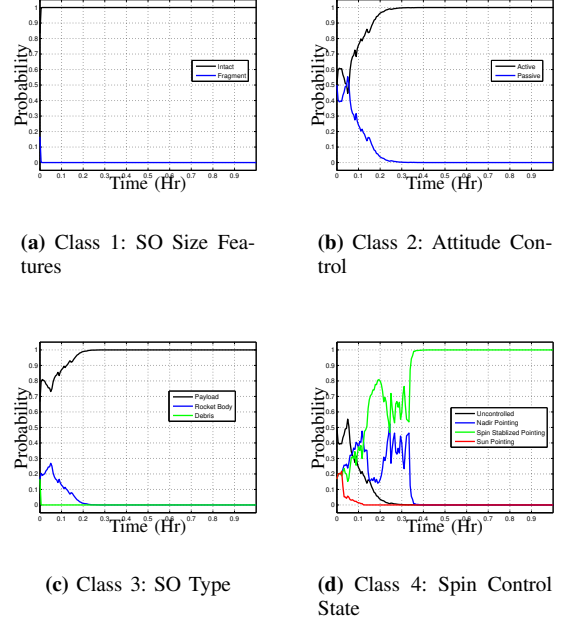


Fig. 5: Spin stabilized Bus Example

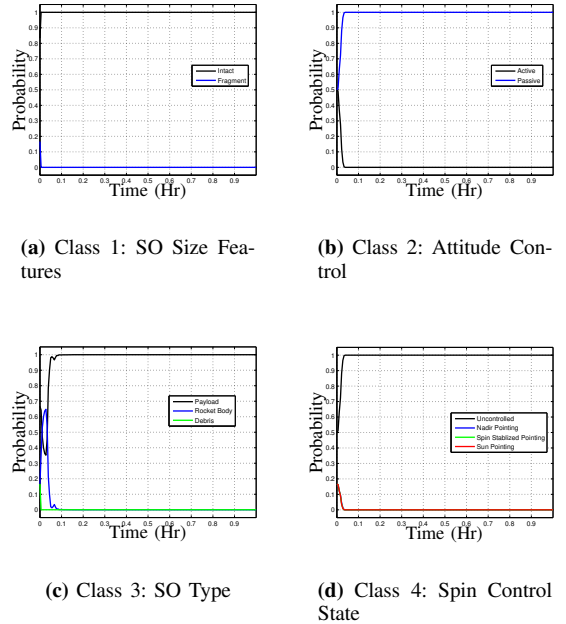


Fig. 6: Uncontrolled Bus Example

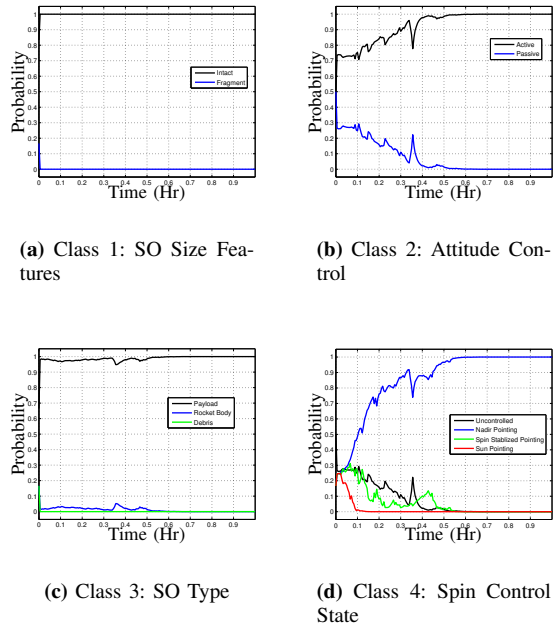


Fig. 7: Nadir Pointing Bus Example

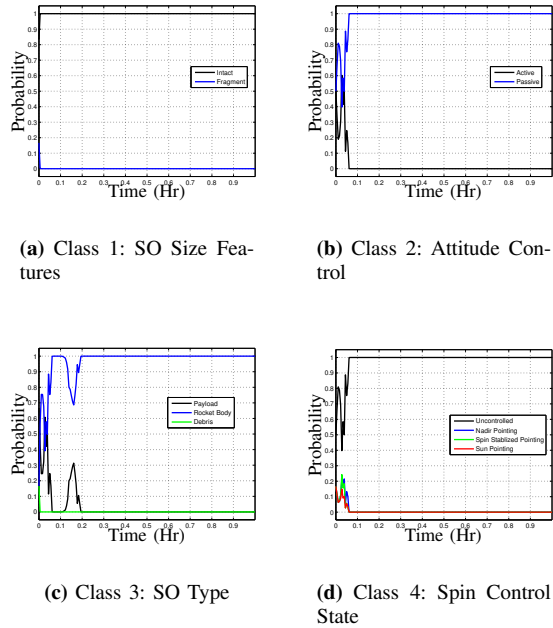


Fig. 8: Rocket Body Example

REFERENCES

- [1] Hinks, J.C., Linares, R., and Crassidis, J.L., "Attitude Observability from Light Curve Measurements," *AIAA Guidance, Navigation, and Control Conference*, AIAA, Boston, MA, Aug. 2013, AIAA Paper #2013-5006.
- [2] Linares, R., Jah, M.K., Leve, F.A., Crassidis, J.L., and Kececy, T., "Astrometric and Photometric Data Fusion For Inactive Space Object Feature Estimation," *Proceedings of the International Astronautical Federation*, Cape Town, South Africa, Sept. 2011, Paper ID: 11340.
- [3] Linares, R., Jah, M.K., Crassidis, J.L., Leve, F.A., and Kececy, T., "Astrometric and Photometric Data Fusion for Inactive Space Object Mass and Area Estimation," *Acta Astronautica*, Vol. 99, June-July 2014, pp. 1–15.
- [4] Linares, R., Jah, M.K., and Crassidis, J.L., "Space Object Area-To-Mass Ratio Estimation Using Multiple Model Approaches," *Advances in the Astronautical Sciences*, Vol. 144, 2012, pp. 55–72.
- [5] Linares, R., Leve, F.A., Jah, M.K., and Crassidis, J.L., "Space Object Mass-Specific Inertia Matrix Estimation From Photometric Data," *Advances in the Astronautical Sciences*, Vol. 144, 2012, pp. 41–54.
- [6] Linares, R., Jah, M.K., Crassidis, J.L., and Nebelecky, C.K., "Space Object Shape Characterization and Tracking Using Light Curve and Angles Data," *Journal of Guidance, Control, and Dynamics*, Vol. 37, No. 1, Jan.-Feb. 2013, pp. 13–25.
- [7] Ashikmin, M. and Shirley, P., "An Anisotropic Phong Light Reflection Model," Tech. Rep. UUCS-00-014, University of Utah, Salt Lake City, UT, 2000.
- [8] Crassidis, J.L. and Markley, F.L., "Unscented Filtering for Spacecraft Attitude Estimation," *Journal of Guidance, Control and Dynamics*, Vol. 26, No. 4, July-Aug. 2003, pp. 536–542.
- [9] Markley, F.L., "Attitude Error Representations for Kalman Filtering," *AIAA Journal of Guidance, Control, and Dynamics*, Vol. 26, No. 2, March-April 2003, pp. 311–317.
- [10] Brown, R.G. and Hwang, P.Y.C., *Introduction to Random Signals and Applied Kalman Filtering*, John Wiley & Sons, New York, NY, 3rd ed., 1997, pp. 353–361.
- [11] Stengel, R.F., *Optimal Control and Estimation*, Dover Publications, New York, NY, 1994, pp. 402–407.
- [12] Anderson, B.D.O. and Moore, J.B., *Optimal Filtering*, chap. 10.1, Dover Publications, Mineola, NY, 2005.
- [13] Anderson, B.D.O., Moore, J.B., and Hawkes, R.M., "Model Approximations via Prediction Error Identification," *Automatica*, Vol. 14, No. 6, Nov. 1978, pp. 615–622.
- [14] Shuster, M.D., "A Survey of Attitude Representations," *Journal of the Astronautical Sciences*, Vol. 41, No. 4, Oct.-Dec. 1993, pp. 439–517.
- [15] Hall, D.T., Africano, J.L., Lambert, J.V., and Kervin, P.W., "Time-Resolved I-Band Photometry of Calibration Spheres and NaK Droplets," *Journal of Spacecraft and Rockets*, Vol. 44, No. 4, July 2007, pp. 910–919.